Hydrogen atom in crossed electric and magnetic fields: Phase space topology and torus quantization via periodic orbits

Stephan Gekle and Jörg Main

Institut für Theoretische Physik 1, Universität Stuttgart, 70550 Stuttgart, Germany

Thomas Bartsch

Department of Mathematical Sciences, Loughborough University, Loughborough LE11 3TU, UK

T. Uzer

Center for Nonlinear Science, Georgia Institute of Technology, Atlanta, Georgia 30332-0430, USA
(Dated: 2nd February 2008)

A hierarchical ordering is demonstrated for the periodic orbits in a strongly coupled multidimensional Hamiltonian system, namely the hydrogen atom in crossed electric and magnetic fields. It mirrors the hierarchy of broken resonant tori and thereby allows one to characterize the periodic orbits by a set of winding numbers. With this knowledge, we construct the action variables as functions of the frequency ratios and carry out a semiclassical torus quantization. The semiclassical energy levels thus obtained agree well with exact quantum calculations.

I. INTRODUCTION

The hydrogen atom in crossed electric and magnetic fields is among the paradigmatic examples of strongly coupled multidimensional systems. During the last two decades, a large number of experimental and theoretical investigations (eg., [1, 2, 3, 4, 5, 6, 7, 8, 9, 10, 11, 12, 13]) have been devoted to the intricate physics of this seemingly elementary nonintegrable system. In addition to its inherent interest, the hydrogen atom in crossed fields can be used to study generic phenomena such as Arnold diffusion [10], monodromy [11] or Ericson fluctuations [12, 13]. Its deeper understanding also provides a solid basis to explore the behavior of confined electrons in condensed matter physics, such as in excitons [14] and quantum dots [15]. Yet, in spite of the large amount of work spent upon it, the overall phase space structure of the crossed-fields hydrogen atom still defies a complete understanding.

One of the most prominent features of a dynamical system are its periodic orbits (POs). While individual POs can yield deep insights into the local dynamics, in their entirety they provide an appropriate tool to understand the global structure of a multidimensional phase space [16]. Their knowledge is crucial in many applications of classical dynamical systems such as astronomy [16, 17, 18], particle accelerators [19] and fluid dynamics, e.g. statistics of turbulent flow [20]. The semiclassical quantization of the classical structures is an invaluable tool for the description of molecular vibrations [21, 22, 23], chemical reactions [24] or the spectra of Rydberg atoms [2, 9].

In this work we establish an organizing principle for POs in the crossed-fields hydrogen atom. It allows the identification of winding numbers for every PO that originates from the breakup of a torus. Conversely, through this classification the POs elucidate the higher-dimensional structures of the phase space and allow one to characterize their topology. They enable us to reconstruct the hierarchy of broken tori with sufficient precision to carry out an Einstein-Brillouin-Keller (EBK) torus quantization [25, 26, 27, 28, 29].

The electron motion of a hydrogen atom exposed to an electric field F in the x direction and a magnetic field B in the z direction, is governed by the Hamiltonian, in atomic units [30],

$$H = \frac{1}{2}\mathbf{p}^2 - \frac{1}{r} + \frac{B}{2}\left(p_y x - p_x y\right) + \frac{B^2}{8}\left(x^2 + y^2\right) - Fx . \quad (1)$$

Here $\mathbf{r} = (x, y, z)$ are the usual Cartesian coordinates, $\mathbf{p} = (p_x, p_y, p_z)$ the conjugate momenta, and $r = \sqrt{x^2 + y^2 + z^2}$. By virtue of the scaling properties [31] of the Hamiltonian (1), if all classical quantities are multiplied by suitable powers of the magnetic field strength, the dynamics can be shown not to depend on the energy E and the field strengths B and F separately, but only on the scaled energy $\tilde{E} = B^{-2/3}E$ and the scaled electric field strength $\tilde{F} = B^{-4/3}F$. In particular, coordinates scale according to $\tilde{\mathbf{r}} = B^{2/3}\mathbf{r}$ and the classical actions obey $\tilde{S} = B^{1/3}S$. In this paper, we present results for a scaled electric field strength $\tilde{F} = 0.5$ and two scaled energies $\tilde{E} = -1.5$ and $\tilde{E} = -1.4$ slightly below and slightly above the classical ionization threshold $\tilde{E}_{\mathrm{I}} = -2\sqrt{\tilde{F}}$, respectively.

The organization of this paper is as follows. In Sec. II we give a brief general review of the phase space structures in Hamiltonian systems that are relevant to our investigations. Sec. III explains the dynamical principles underlying the organization of periodic orbits and summarizes the organization of periodic orbits of the hydrogen atom in crossed electric and magnetic fields. In Sec. IV we describe this organization in detail and show how it can be exploited to assign winding numbers to the

periodic orbits. Sec. V presents the calculation of action variables from the information thus obtained. A semi-classical Einstein-Brillouin-Keller quantization is carried out in Sec. VI, and conclusions are given in Sec. VII.

II. PHASE SPACE STRUCTURES IN HAMILTONIAN SYSTEMS

Among all Hamiltonian systems, those that exhibit the most regular dynamics are the integrable systems, where almost every bounded trajectory is confined to an invariant torus. At the other extreme, in ergodic systems almost every trajectory comes arbitrarily close to every energetically allowed point in phase space. In this work we treat the crossed-fields hydrogen atom in a parameter range where the phase space structure is dominated by the remnants of invariant tori. Nevertheless, the external fields are chosen too strong for perturbation theory to be a reliable tool, and we will consider the full nonintegrable Hamiltonian (1).

By definition, a Hamiltonian system with f degrees of freedom is integrable if it possesses f constants of motion in involution. The regular level sets of these constants are f-dimensional tori if they are compact [32, 33]. For singular values of the constants, tori of lower dimensions can arise. Tori of different dimensions form a hierarchy in which the tori of dimension N are organized around the tori of dimension $N-1$. Such hierarchies have been observed in a variety of different systems (see, e.g., [11, 21, 34]). In the following sections, we will demonstrate how this hierarchy of tori in an integrable limit can give rise to a hierarchy of isolated POs in a nonintegrable system and how these POs can in turn be used to gain information on the original hierarchy of invariant tori.

In an integrable system, action-angle variables $(\mathbf{I}, \boldsymbol{\theta})$ with the following properties can be introduced. The angles $\boldsymbol{\theta}$ determine the position on an individual torus. They increase linearly with time

$$\boldsymbol{\theta} = \boldsymbol{\omega} t + \boldsymbol{\theta}_0, \tag{2}$$

with a constant frequency vector $\boldsymbol{\omega}$ and initial conditions $\boldsymbol{\theta}_0$. The conjugate action variables $\mathbf{I}$ are constants of motion and characterize the invariant tori. They are given by

$$I_i = \frac{1}{2\pi} \oint_{\gamma_i} \mathbf{p} d\mathbf{q}, \tag{3}$$

where γ_i is the loop on the torus obtained as the angle θ_i varies from 0 to 2π with all other angles held fixed.

The action variables (3) form the basis for a semi-classical torus quantization [25, 26, 27, 28, 29]. Finding them explicitly, however, is a highly nontrivial task. Due to its significance in applications such as the calculation of molecular vibration spectra, the construction of the invariant tori has attracted considerable attention [35, 36, 37].

In an integrable system, the Hamiltonian can be written as a function of the action variables only, and the frequencies $\boldsymbol{\omega}$ in (2) are given by

$$\omega_i = \frac{\partial H}{\partial I_i}. \tag{4}$$

If the ratios of any two of the ω_i on a torus are rational, that torus carries periodic orbits and is called a resonant torus. In this case, a set $\mathbf{w}$ of integer winding numbers can be found so that

$$\omega_1 : \omega_2 : \ldots : \omega_n = w_1 : w_2 : \ldots : w_n. \tag{5}$$

Each winding number w_i specifies the number of rotations along the direction of the fundamental loop γ_i that the POs execute before repeating themselves.

Angle coordinates $\boldsymbol{\theta}$ on a given torus can be defined in various ways. Apart from a choice of origin, which is inconsequential, any two angle coordinate systems are related by a linear transformation

$$\boldsymbol{\theta}' = M \cdot \boldsymbol{\theta} \tag{6}$$

where M is an $n \times n$ integer matrix with unit determinant [38]. The action coordinates must be transformed according to

$$\mathbf{I}' = (M^{\mathrm{T}})^{-1} \cdot \mathbf{I}, \tag{7}$$

whereas the winding numbers on a rational torus transform as

$$\mathbf{w}' = M \cdot \mathbf{w}. \tag{8}$$

This freedom to choose different action-angle coordinate systems, together with the intimate connection between coordinate systems and winding numbers, will play a crucial role in our investigation of the phase space topology.

In a non-integrable system, a resonant torus breaks up into isolated POs [32, 39, 40]. We use these POs as representatives of the torus they stem from and call them N-torus POs, where N is the dimension of the original torus. According to Kolmogorov-Arnold-Moser (KAM) theory [32, 33], most nonresonant tori remain intact in a near-integrable system and break up only gradually. They are interspersed with the isolated POs in the same way as resonant and nonresonant tori are interspersed in an integrable system. Therefore, POs can be used to investigate the structure of the surviving tori.

According to the Poincaré-Birkhoff theorem [32, 33, 39], a 2-torus in a two-degree-of-freedom system breaks up into an even number of isolated POs, usually two. One of the POs is stable ("elliptic"), the other is unstable ("hyperbolic"). Because both POs stem from the same torus, their periods and actions differ only slightly.

For systems with three degrees of freedom, Kook and Meiss [40] were able to derive from symmetry considerations that a 3-torus breaks up into four isolated POs that usually represent the four possible stability combinations: one PO elliptic in both degrees of freedom (ee), one PO hyperbolic in both degrees of freedom (hh) and two POs elliptic in one degree of freedom and hyperbolic in the second (eh and he).
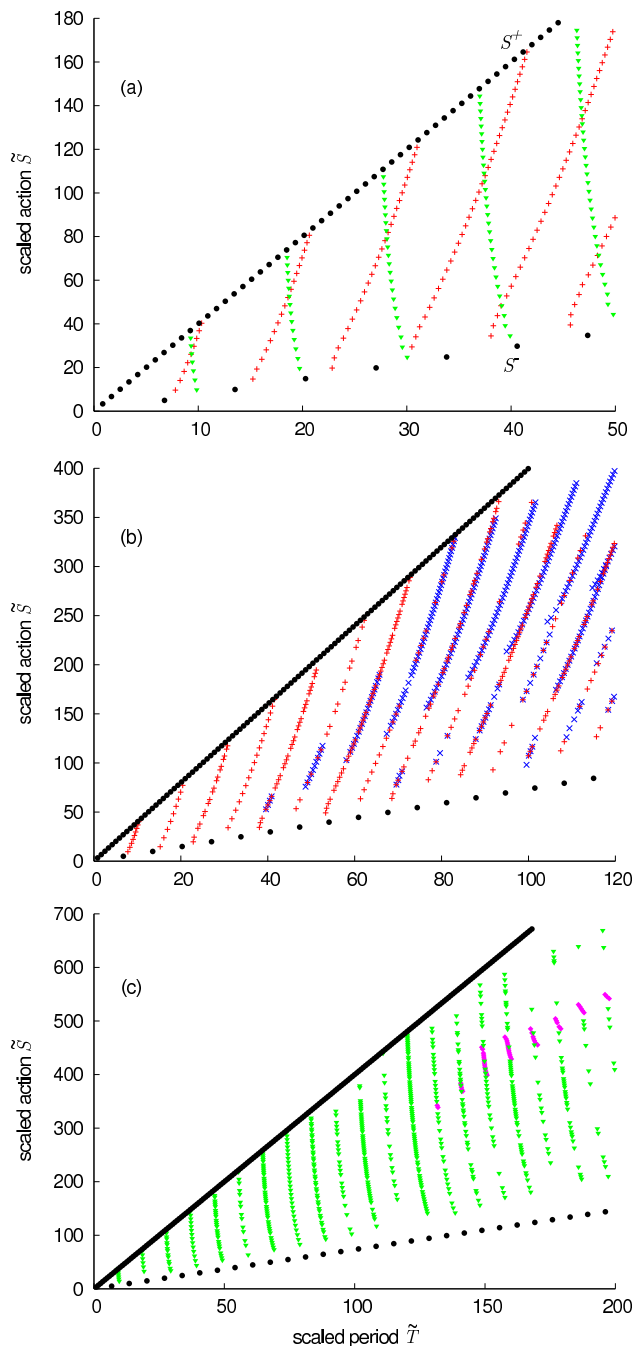
Figure 1: Periodic orbits at $\tilde{E} = -1.4$ and $\tilde{F} = 0.5$. The FPOs $S^{\pm}$ and their repetitions are shown with black circles. (a) the 2-torus POs T_2^{p} (red plus symbols) and T_2^{n} (green triangles). (b) the T_2^{p} and their 3-torus partners T_3^{p} (blue crosses). (c) the T_2^{n} and their 3-torus partners T_3^{n} (magenta diamonds).
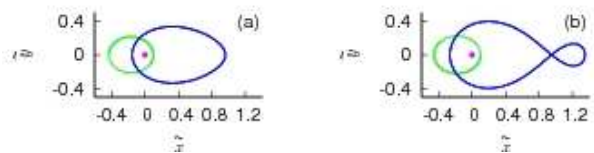
Figure 2: The two planar FPOs S^{+} (green) and S^{-} (blue) at $\tilde{E} = -1.5$ (a) and $\tilde{E} = -1.4$ (b), where S^{-} is already strongly deformed. The position of the nucleus is marked by a dot.

Several such lists are available in the literature (see, e.g., [2, 4, 5, 9]), but no comprehensive ordering scheme for POs in three degrees of freedom has been proposed so far, and *a priori* it is not even clear if one exists. However, in Fig. 1 a clear structure underlying the family of POs becomes apparent: The periods and actions of most POs fall into well-separated series. (A few orbits that arise from secondary bifurcations and do not fit this pattern were omitted from the figure.) In a recent publication [41] we argued that the POs arise from the breakup of invariant tori (i.e., they are N-torus POs in the terminology of Sec. II) and that the series structure provides evidence for a hierarchical ordering of POs that reflects the hierarchy of invariant tori in an integrable limit of the dynamics. In the following, we will briefly summarize the conclusions reached in [41], describe in detail the computational procedures that justify them and demonstrate how the ordering of POs can be used to gain insight into the topology of higher-dimensional phase space structures. In the course of the exposition, the nomenclature used in Fig. 1 will be made clear.

The three shortest or fundamental periodic orbits (FPOs) of the crossed-fields hydrogen atom were found in [4, 5]. They do not arise from the breakup of a higher-dimensional torus and therefore represent the 1-torus POs in the hierarchy. Two of these, labeled S^{+} and S^{-} in [5], serve as organizing centers for the entire hierarchy. Both of them are planar. They are depicted in Fig. 2. For very low energies, S^{+} and S^{-} are shaped like Keplerian ellipses [4]. At the energy levels chosen in this work, S^{+} maintains this form, whereas S^{-} is strongly deformed as shown in Fig. 2. In addition, above the ionization threshold the FPO S^{-}, although still stable, is surrounded by a phase space region of ionizing trajectories [6, 8, 42].

The mechanism that enables the FPOs to organize the hierarchy of N-torus POs around them can best be illustrated if the discussion is temporarily restricted to the $\tilde{x}$-$\tilde{y}$ plane perpendicular to the magnetic field. This plane forms an invariant two-dimensional subsystem. Its dynamics is therefore accessible to an investigation using a Poincaré surface of section such as Fig. 3. The plot shows the two FPOs S^{+} and S^{-}, each at the center of an island of stability. They are surrounded by POs of larger periods. In an obvious way, the latter can be thought of as arising from the breakup of resonant invariant tori and being interleaved with surviving KAM tori as described

III. ORGANIZATION OF PERIODIC ORBITS

Our investigation of the POs in the crossed-fields hydrogen atom starts with a numerical search for periodic orbits. This search, which is described in detail in Appendix A, produces a long and unstructured list of POs.
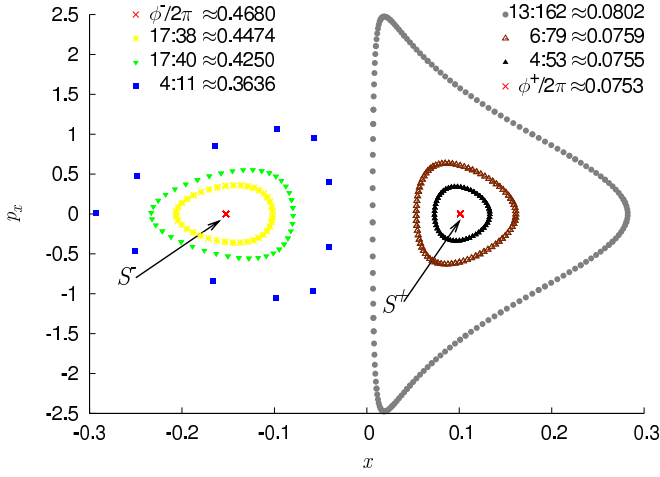
Figure 3: Periodic orbits in the Poincaré surface of section $\tilde{y} = 0$ for the planar subsystem, $\tilde{E} = -1.5$, $\tilde{F} = 0.5$. Non-fundamental POs are labeled by their winding ratios.

Figure 4: The hierarchy of N-torus POs in the crossed-fields hydrogen atom at $\tilde{E} = -1.5$, $\tilde{F} = 0.5$ (and at $\tilde{E} = -1.4$, $\tilde{F} = 0.5$, except for the collapse on S^-). The two families of 3-torus POs T_3^{p} and T_3^{n} collapse onto their 2-torus partners T_2^{p} and T_2^{n} as $\tilde{I}_3 \to 0$. The T_2 in turn collapse onto the FPOs S^+ and S^-. For a correct description of the collapse the appropriate coordinate system must be used: $\tilde{I}_1 \to 0$ for S^- and $\tilde{I}_1' \to 0$ for S^+. The coordinate change is described by the topological invariants M^{p} and M^{n}.

in the previous section. Therefore, the POs can be labeled with winding numbers and action variables that stem from the original family of invariant tori, and thus provide access also to the distribution of the remaining invariant tori, which are much harder to compute.

An integrable Hamiltonian system with $f > 2$ degrees of freedom possesses an entire hierarchy of invariant tori of dimensions up to f. In every dimension the fully resonant tori break up into isolated POs. A generic higher-dimensional Hamiltonian system will therefore exhibit a hierarchy of N-torus POs, where at each level the family of N-torus POs is organized by the underlying family of $(N-1)$-torus POs. This scenario is entirely analogous to the simple two-dimensional example of Fig. 3, but beyond two degrees of freedom we cannot rely on Poincaré surface of section plots to diagnose the situation.

In Fig. 1 all series end at lines that are formed by the FPOs and their repetitions. This observation gives us a first hint that the FPOs indeed serve as organizing centers for the families of longer POs even in the full, three-dimensional dynamics. This hint, however, is weak, and it is desirable to characterize the relation between the FPOs and the families they organize in a more detailed way.

In Ref. [41], we proposed three quantitative criteria to this end: (i) The stability angles $\phi_1^{\pm}$ of the FPOs $S^{\pm}$ (i.e. the phase angles of the unimodular eigenvalues of their stability matrices) describe the rotation that each FPO imposes upon its neighborhood. The winding ratios of the 2-torus POs converge toward $\phi_1^{\pm}/2\pi$ as the FPOs are approached. (ii) In the same limit, the action variable corresponding to the degree of freedom along the FPO converges to the action of the FPO, and (iii) the action variable for the motion transverse to the FPO, which is given by the area the (original) invariant torus encloses in the Poincar plane, tends to zero. We will use these criteria, which are derived in a two-dimensional setting,
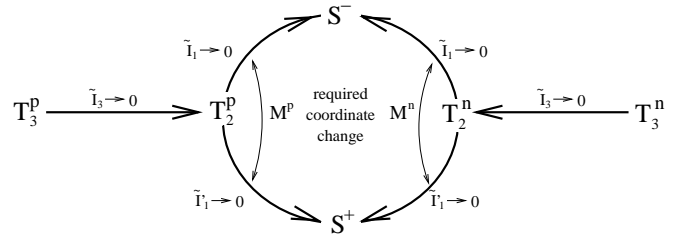
more generally to characterize the relationship between the N-torus POs at different levels of the hierarchy.

The entire hierarchy of POs that will be reconstructed with the help of these criteria is illustrated in Fig. 4. We distinguish between two families T^{p} and T^{n} of N-torus POs that appear as series with positive (p) or negative (n) slope, respectively, in Fig. 1. Each of these contains a family $T_2^{\mathrm{p,n}}$ of 2-torus POs and a family $T_3^{\mathrm{p,n}}$ of 3-torus POs. Since POs which are remnants of the same torus have nearly identical scaled actions $\tilde{S}$ and periods $\tilde{T}$, each point in Fig. 1 represents one specific broken torus. The FPOs S^+ and S^- serve as organizing centers for both families T_2^{p} and T_2^{n} of 2-torus POs. The POs located in the $\tilde{x}$-$\tilde{y}$ symmetry plane (and shown in Fig. 3) form the family T_2^{p}. The 2-torus POs themselves are found to be limiting cases of two families T_3^{p} and T_3^{n} of 3-torus POs.

To justify this description of the hierarchy, it is necessary to assign winding numbers to individual POs and calculate the corresponding action variables, so that the three criteria can be applied. These calculations will be presented in Sec. IV and V. It will also be shown that the freedom of choice in the definition of action-angle coordinate systems that was explained in Sec. II and that at first sight seems to impede the application of the criteria can in fact be used to assign winding numbers to each torus in the coordinate system that is best adapted to the local dynamics. The way how different local coordinate systems transform into one another then contains global information about the topology of the families of invariant tori that is represented by the topological invariants M^{p} and M^{n} in Fig. 4.

IV. ASSIGNMENT OF WINDING NUMBERS

A. The 2-torus POs T_2^{p} and T_2^{n}

Winding numbers for the 2-torus POs T_2^{p} and T_2^{n} can be assigned as follows: counting the series in Fig. 1 (a)

yields the first winding number w_1. Counting the POs within one series from bottom to top yields the second winding number w_2. The first series must be assigned $w_1 = 1$ because the repetitions of the orbits in the leftmost series occur in all higher series and the k-fold repetition of a PO results in another PO with winding numbers multiplied by k compared to the primitive PO.

Using the same multiplication principle, we can perform a first consistency check on this numbering scheme because it allows us to derive a pattern for the values of w_2 across different series. All POs in the first series are obviously primitive, whereas in higher series primitive and repeated POs are interleaved. As illustrated in Fig. 5, the winding numbers of all orbits in the higher series can be deduced from those of the first series. The numerical results shown in Fig. 6 confirm this pattern. Only the base value w_2^0 to be assigned to the PO with the lowest action in the first series remains undetermined from these considerations. It will turn out that w_2^0 cannot be determined uniquely. Instead, different subsets of POs suggest different values of the winding number w_2. As will be explained below, this non-uniqueness reflects the freedom of choice of different action-angle coordinate systems and allows one to assign winding numbers to each torus in the coordinate system that is best adapted to the local dynamics.

To determine w_2^0 we use a Fourier series expansion of the time series of the Cartesian coordinates, with the frequencies $\tilde{\omega}$ measured in units of the fundamental frequency $\tilde{\omega}_0 = 2\pi/\tilde{T}$. For a PO with period $\tilde{T}$, these Fourier spectra do not show peaks at all multiples of the

fundamental frequency, but only at those that correspond to the winding numbers and some of their integer linear combinations [37]. For the planar T_2^{p} family it suffices to consider $\tilde{x}(\tilde{t})$, since the spectra for $\tilde{y}(\tilde{t})$ show peaks at identical positions. The first peak at $\tilde{\omega} = 1 \cdot \tilde{\omega}_0$ in the example of Fig. 7 corresponds to the series number w_1 of the POs. It is found in the same position for any PO in a given series. The second major peak corresponds to the second winding number w_2. Fig. 7(a) shows the spectrum for the PO with the lowest action in the first series, where this second peak is located at $\tilde{\omega} = 2 \cdot \tilde{\omega}_0$.

We can therefore set $w_2^0 = 2$, which according to Fig. 5 determines the values of w_2 for all orbits. However, as

Figure 6: The pattern of primitive and repeated POs for the first four series of the T_2^{p} (a) and the T_2^{n} (b). POs in the first series and their repetitions are shown with red circles, POs in the second series and their repetitions with green diamonds and POs from the third and fourth series in blue squares and black triangles, respectively. The sequence of primitive and repeated POs within the individual series should be compared to the pattern shown in Fig. 5, which was derived from the multiplication principle. The numerical results agree perfectly with the theoretical predictions.
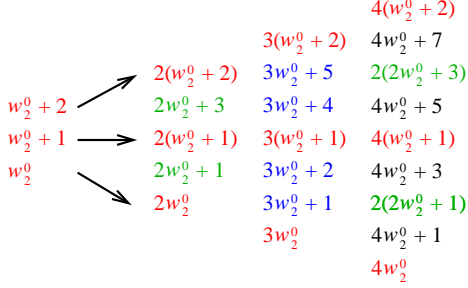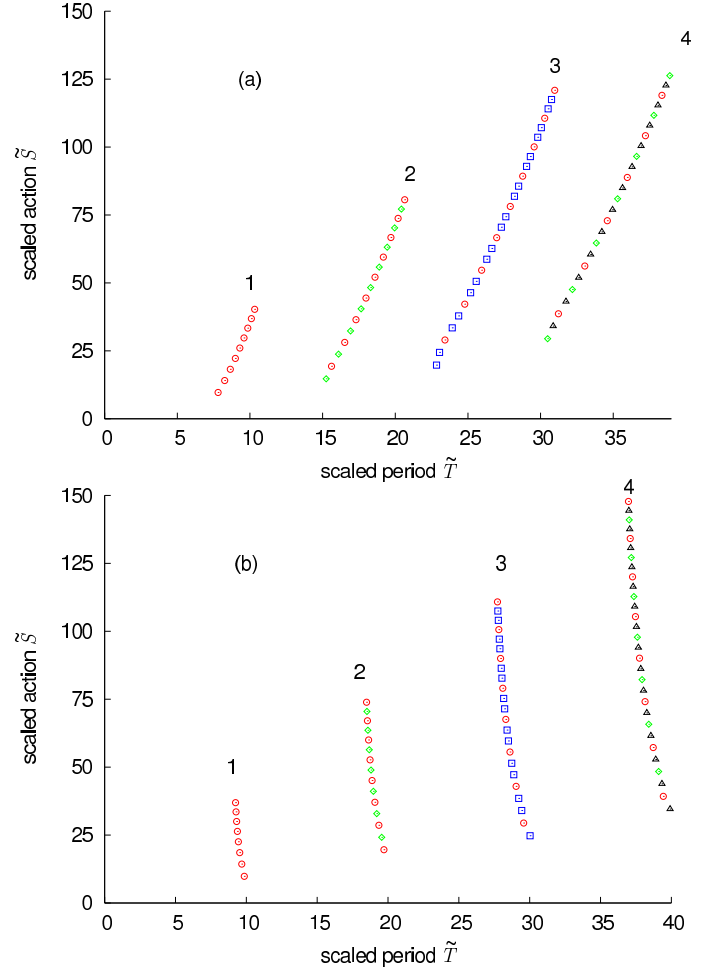

Figure 5: The pattern of primitive and repeated POs for the first four series of 2-torus POs derived theoretically. The first series $w_1 = 1$ contains only primitive POs. The second series $w_1 = 2$ shows an alternating sequence of primitive POs (odd w_2) and repetitions of the POs in the first series (even w_2). (It cannot be derived from the multiplication principle if there is an additional primitive PO at the lower or upper end of the second series.) In the third series there are blocks of two primitive POs (w_2 indivisible by 3) separated by 3-fold repetitions of the first series POs (w_2 divisible by 3). The fourth series contains primitive POs for odd values of w_2, 4-fold repetitions of the first series for positions with w_2 divisible by 4 and 2-fold repetitions of the second series for w_2 divisible by 2 but not by 4. The scheme can be extended to arbitrarily large values of w_1.
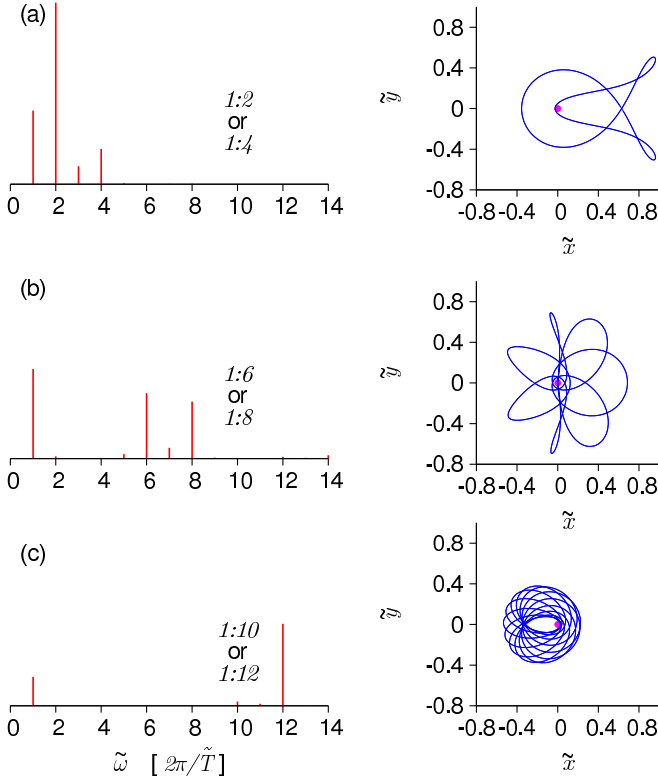
Figure 7: Fourier spectra (absolute values of Fourier coefficients) of $\tilde{x}(\tilde{t})$ for some POs of the T_2^{p} family. Orbits are labeled by winding numbers calculated in two different coordinate systems (see text). The right column shows the orbits in configuration space and the position of the nucleus.

Figure 8: Fourier expansions of $\tilde{x}(\tilde{t})$ (red) and $\tilde{z}(\tilde{t})$ (green) for POs from the T_2^{n} family. Peaks not associated with winding numbers are located at integer linear combinations thereof [37].

Fig. 7(b) and (c) show, the peak corresponding to this value of w_2 is not always dominant and can indeed be very weak if w_2 is large. Instead, a strong peak arises at a different position and suggests choosing a different set of winding numbers that has $w_2^{0\prime} = 4$ and is connected to the previous system by the transformation

$$
\begin{aligned}
w_1' &= w_1, \\
w_2' &= 2w_1 + w_2.
\end{aligned}
\tag{9}
$$

Both choices are equally viable. They correspond to different choices of angle coordinates on the original tori. As the Fourier spectra illustrate, the "unprimed" coordinate system is well adapted to the dynamics of orbits with low values of w_2, whereas the "primed" coordinates describe the dynamics of orbits with high w_2.

In view of Fig. 1 (a) it is evident that POs with low w_2 lie close to S^-, while POs with high w_2 are close to S^+. The transition indicates that the dominant modes of the dynamics change from one end of the series to the other: close to S^-, these normal modes are the motion parallel and transverse to the FPO. As the distance from S^- grows, the coupling of the normal modes increases, and as S^+ is approached, the normal modes imposed by that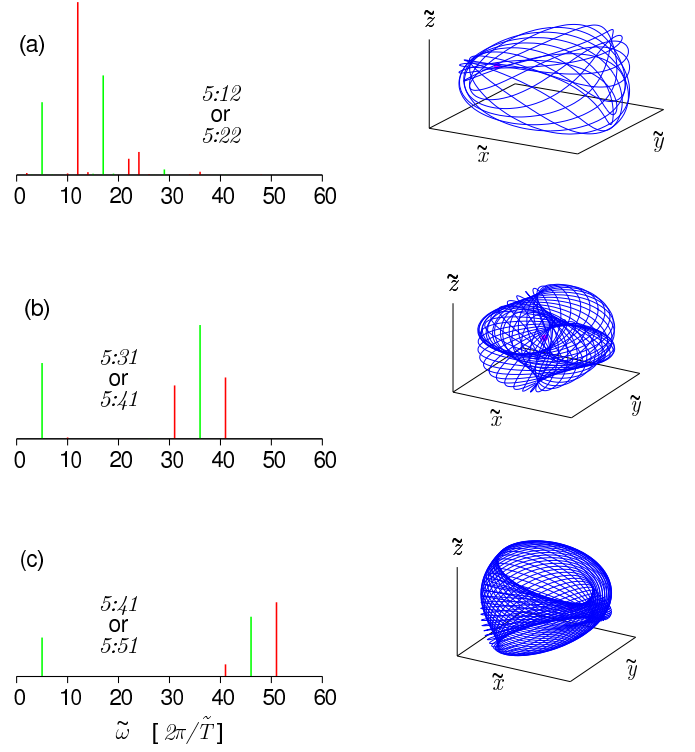 FPO, which are different, gain dominance. In this way, the two FPOs that bound the T_2^{p} family impose two different systems of angle coordinates $\boldsymbol{\theta}$ and $\boldsymbol{\theta}'$ on the tori in their neighborhood. The transformation between the two coordinate systems is a topological invariant that characterizes the family of 2-torus POs. In our case, it is given by Eq. (9) and characterized by the matrix

$$
M^{\mathrm{p}} = \begin{pmatrix} 1 & 0 \\ 2 & 1 \end{pmatrix}.
\tag{10}
$$

As anticipated in Sec. II, M^{p} is an integer matrix with unit determinant.

Using a similar method, one can assign winding numbers to the POs of the T_2^{n} family. These POs are not restricted to the x-y symmetry plane, they are truly three-dimensional in Cartesian coordinate space, so that a Poincaré surface of section plot similar to Fig. 3 cannot be obtained. Nevertheless, the Fourier spectra of $\tilde{x}(\tilde{t})$ and $\tilde{z}(\tilde{t})$ provide the information needed for a complete assignment of winding numbers, as shown in Fig. 8. It is again found that the dominant normal modes are different for POs at the lower end of the series, close to S^-, and at the upper end of the series, close to S^+. The invariant $M^{\mathrm{n}} = M^{\mathrm{p}}$ that characterizes the transition between the two limits takes the same value for both families.

B. The 3-torus POs T_3^{p} and T_3^{n}

Apart from the 2-torus POs, Fig. 1 (b) and (c) show POs that are generated in the destruction of 3-tori. They are arranged in the same series as the 2-torus POs, and each 3-torus PO is intimately related to a 2-torus "partner" with almost identical period and action. Such partners have identical winding numbers w_1 and w_2, but 3-torus POs possess a third winding number w_3, which distinguishes different 3-torus PO partners of the same 2-torus PO. It manifests itself in an additional peak in the Fourier spectra and can therefore be assigned by a straightforward extension of the technique used to classify the 2-torus POs. For the T_3^{n} as in Fig. 9 (a) and (b) the situation is unambiguous since there is only one strong additional peak. The location of this peak provides the winding number w_3. For POs of the T_3^{p} family (see Fig. 9 (c) and (d)), however, two additional peaks of comparable magnitude arise, giving us two possibilities to assign the third winding number. In Fig. 9 (d), the two possibilities are $w_3 = 5$ and $w_3' = 1$. As for the 2-torus POs, the two systems of winding numbers correspond to different angle coordinate systems on the original tori. In our case, the transformation between the two systems is given by:

$$w_3' \;=\; w_1 - w_3. \tag{11}$$

Note that there is no obvious relation between the classification by winding numbers that becomes possible though the present analysis and the geometrical appearance of the POs in configuration space.

C. The stability of the POs

The stability of a PO in a Hamiltonian system with three degrees of freedom is characterized by a 4×4 symplectic stability matrix, which describes the linearized dynamics transverse to the PO [32, 40, 43]. Because the stability matrix is real and symplectic, with each eigenvalue λ its inverse $1/\lambda$ and its complex conjugate λ^* must also be eigenvalues. Therefore, if the eigenvalues of the stability matrix are different from ± 1, they must belong to either (i) an elliptic pair $e^{\pm i\varphi}$ of complex conjugate eigenvalues with unit modulus, (ii) a hyperbolic pair λ, $1/\lambda$ of real eigenvalues, or (iii) a loxodromic quartet λ, $1/\lambda$, λ^*, $1/\lambda^*$ of complex eigenvalues. A PO is stable if and only if all eigenvalues of its stability matrix have unit modulus.

On an N-dimensional resonant torus in an integrable system, POs occur in continuous N-parameter families. They therefore have marginal stability, i.e., all four eigenvalues of their stability matrix equal one. In a nonintegrable system only a small number of isolated POs remains. The eigenvalues of their stability matrix occur in elliptic (e) or hyperbolic (h) pairs. In our numerical studies we did not find any loxodromic quartets for
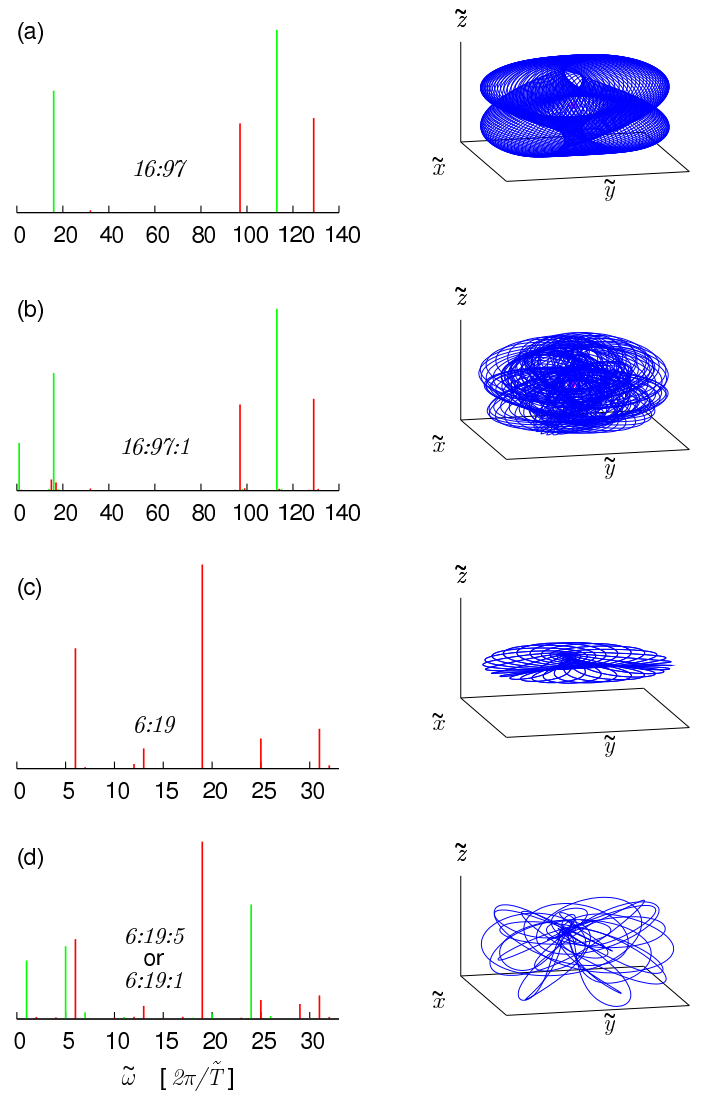

Figure 9: Fourier spectra of $\tilde{x}(\tilde{t})$ (red) and $\tilde{z}(\tilde{t})$ (green). The second winding number is given in the unprimed coordinate system $w_2^0 = 2$. (a) A 2-torus PO in the T_2^{n} family and (b) its 3-torus partner from T_3^{n}. (c) A 2-torus PO from the T_2^{p} family and (d) its 3-torus partner from T_3^{p}.

N-torus POs. In some cases our search algorithm finds a large number of POs all of which originate from the breakup of the same torus and have almost marginal stability. In these cases, the splitting of the original torus is so small that we cannot resolve isolated POs within the given numerical precision. In the other cases, whenever our numerical PO search allows us to identify all members in a quadruplet resulting from the breakup of a 3-torus, we find that it contains all four stability combinations ee, eh, he and hh, in accordance with [40].

The 2-torus POs occur as doublets, of which Fig. 10 shows an example. One pair of stability eigenvalues is approximately the same for both members of a doublet. It corresponds to the motion transverse to the original
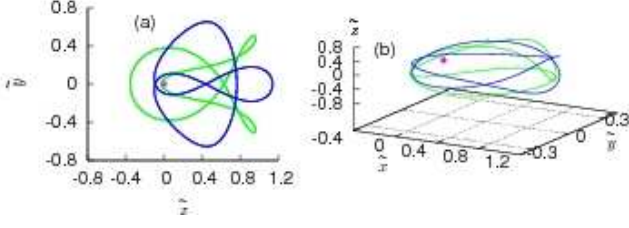
Figure 10: Elliptic (green) and hyperbolic (blue) POs with winding numbers 1:2 (a) in the T_2^{p} family and (b) in the T_2^{n} family.

torus. With very few exceptions, the dynamics in this direction is stable. In the direction along the original torus one partner is elliptic while the other is hyperbolic in accordance with the situation of the Poincaré-Birkhoff theorem [39] in two degrees-of-freedom. Figs. 7, 8, 9 show elliptic (e) POs for the T_2 and completely elliptic (ee) for the T_3 in those cases where isolated POs can be identified.

D. Symmetry considerations

The Hamiltonian (1) possesses three discrete symmetries, namely the reflection symmetry with respect to the x-y plane (z-parity), the y-parity with additional time reversal and the combination of both. Due to the z-parity, the x-y plane constitutes a two-degree-of-freedom subsystem. Any PO outside this plane must either be itself invariant under the symmetry transformation or possess a partner related to it via the symmetry transformation.

We find the following connection between winding numbers and symmetry: A PO in the T_3^{p} family is symmetric under the z-parity transformation if and only if its winding numbers w_1 and w_2 are even. In the T_2^{n} and T_3^{n} families, the POs with w_1 odd and w_2 even are symmetric under z-parity, while all others are not. For both families of 3-torus POs the third winding number w_3 has no influence on the symmetry properties.

V. CALCULATION OF ACTION VARIABLES

In this section we compute the scaled action variables $\tilde{\mathbf{I}}$ for each family of POs.

The total action of a PO can be expressed in terms of the individual actions $\tilde{\mathbf{I}}$:

$$\tilde{S} = \mathbf{w} \cdot \tilde{\mathbf{I}}\left(\mathbf{w}\right). \tag{12}$$

For any multiple α of the PO, this becomes:

$$\alpha\tilde{S} = \alpha\mathbf{w} \cdot \tilde{\mathbf{I}}\left(\alpha\mathbf{w}\right), \tag{13}$$

with the same action variables $\tilde{\mathbf{I}}(\alpha\mathbf{w}) = \tilde{\mathbf{I}}(\mathbf{w})$ as before. Thus, the $\tilde{\mathbf{I}}$ for the T_3 families can be written as functions of any two frequency ratios (which by virtue of Eq. (5)

equal the ratios of the winding numbers). Here we choose

$$\tilde{\mathbf{I}}\left(w_1, w_2, w_3\right) = \tilde{\mathbf{I}}\left(\frac{w_1}{w_2}, \frac{w_3}{w_2}\right). \tag{14}$$

To calculate the action variables $\tilde{\mathbf{I}}$ numerically we select three POs close to each other in the $(w_1/w_2,\ w_3/w_2)$ plane, so that the action variables are approximately constant in the small triangular area in between. Under this assumption, we obtain a system of equations

$$
\begin{aligned}
\tilde{S}^{(1)} &= w_1^{(1)}\tilde{I}_1 + w_2^{(1)}\tilde{I}_2 + w_3^{(1)}\tilde{I}_3, \\
\tilde{S}^{(2)} &= w_1^{(2)}\tilde{I}_1 + w_2^{(2)}\tilde{I}_2 + w_3^{(2)}\tilde{I}_3, \\
\tilde{S}^{(3)} &= w_1^{(3)}\tilde{I}_1 + w_2^{(3)}\tilde{I}_2 + w_3^{(3)}\tilde{I}_3,
\end{aligned}
\tag{15}
$$

which can be solved for $\tilde{I}_1$, $\tilde{I}_2$, and $\tilde{I}_3$. These values are then assigned to be the function values at the barycenter of the triangle. The process is repeated for all POs in the corresponding family and the results are used to calculate an interpolation function using a modified Shepard's method [44].

For the 2-torus POs we follow a similar procedure, except that we need to consider only a single winding ratio w_1/w_2. At the energy $\tilde{E} = -1.5$, we thus obtain the results shown in Fig. 11 (a), which also displays the actions and stability angles $\phi_{1,2}$ of the FPOs. The limiting values for high frequency ratios of the T_2^{p} and T_2^{n} families coincide with $\phi_1/2\pi$ and $\phi_2/2\pi$ of S^-, respectively. At the same time, the action variable $\tilde{I}_2$ converges toward the action of the FPO S^-, whereas the action variable $\tilde{I}_1$ vanishes. According to the three criteria listed in Sec. III, we can thus conclude that S^- serves as an organizing center for both families T_2^{p} and T_2^{n} and that the action variable $\tilde{I}_2$ and $\tilde{I}_1$ correspond to the normal modes along and transverse to S^-. (Notice that in three degrees of freedom a stable FPO has two pairs of unimodular stability eigenvalues, so that the collapse scenario of Fig. 3 can take place in two transverse degrees of freedom independently, giving rise to two families of 2-torus POs.) For the planar family T_2^{p}, this result merely confirms the conclusion that we could already draw from the Poincaré surface of section plot in Fig. 3. By contrast, the family T_2^{n}, although it consists of 2-torus POs, is not contained in any two-dimensional subsystem that could be described without an intimate study of the dynamics. Its analysis is therefore beyond the reach of a Poincaré plot. Nevertheless, 11(a) demonstrates that the relations of the families T_2^{p} and T_2^{n} to the FPO S^- are entirely analogous and that S^- organizes T_2^{n} just as much as T_2^{p}.

As described in Sec. IV A, the winding numbers $\mathbf{w}$ used in Fig. 11 (a) are ill-suited to describe the approach to S^+, and the winding numbers $\mathbf{w}'$ given by (9) should be used instead. Indeed, none of the actions $\tilde{I}_1$ and $\tilde{I}_2$ tends to zero in the limit of low frequency ratios. Nevertheless, S^+ can be located in Fig. 11 (a) if its stability angles ϕ', which naturally arise in the $\mathbf{w}'$ system, are transformed to the $\mathbf{w}$ system just as if they were regular frequency
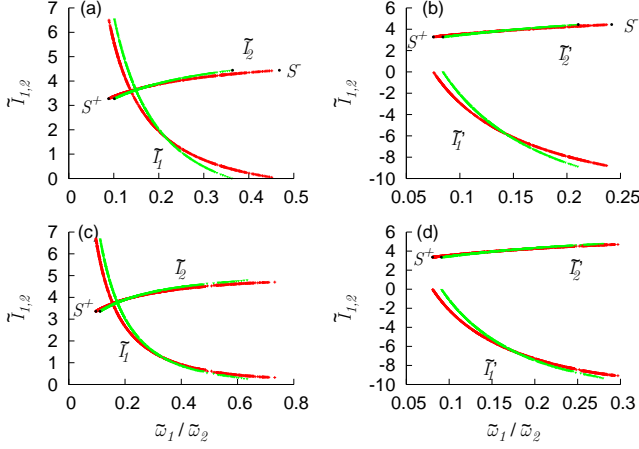
Figure 11: The actions $\tilde{I}_1$ and $\tilde{I}_2$ for the T_2^{p} (red plus symbols) and T_2^{n} (green triangles). (a) Actions at $\tilde{E} = -1.5$, $\tilde{F} = 0.5$ in the unprimed action-angle coordinate system with $w_2^0 2$. The winding numbers are suitable to describe the approach to S^-, where $\tilde{I}_1$ tends to zero. The stability angles of the FPO S^+ have been transformed using Eq. (17). (b) The same data in the primed coordinate system with $w_2^0 = 4$. The situation around the FPOs is reversed. (c) Actions at $\tilde{E} = -1.4$, $\tilde{F} = 0.5$ (unprimed coordinates). The $T_2^{\mathrm{p,n}}$ do not collapse onto S^- due to the ionizing region around that FPO. (d) Actions at $\tilde{E} = -1.4$, $\tilde{F} = 0.5$ (primed coordinates).

ratios by applying the inverse transformation of (9):

$$\frac{w_1}{w_2} = \frac{w_1'}{w_2' - 2w_1'} = \frac{\frac{w_1'}{w_2'}}{1 - 2\frac{w_1'}{w_2'}} \qquad (16)$$

and therefore

$$\frac{\phi}{2\pi} = \frac{\frac{\phi'}{2\pi}}{1 - 2\frac{\phi'}{2\pi}}. \qquad (17)$$

The transformed stability angles ϕ in Fig. 11 (a) demonstrate that the $T_2^{\mathrm{p,n}}$ emanate from S^+ just as they emanate from S^- in the limit of high winding ratios. This result can be illustrated more clearly if the actions are calculated in the $\mathbf{w}'$ coordinate system, as shown in Fig. 11(b). Here, the situation around the FPOs reverses: $\tilde{I}_1'$ tends to zero as S^+ is approached and remains finite in the vicinity of S^-. (Note that by virtue of Eq. (7) there can exist coordinate systems in which the action variables take negative values.) In Fig. 11(b), the true stability angles of S^+ can be used to indicate the lower limits of the winding ratios, whereas the stability angles of S^- need to be transformed with the inverse of Eq. (17).

This symmetry demonstrates that locally the collapse of the $T_2^{\mathrm{p,n}}$ onto S^+ and S^- looks the same when described in suitable local coordinates. The nontrivial topology of the families T_2^{p} and T_2^{n} that is represented by the invariants $M^{\mathrm{p,n}}$ becomes visible only if the entire families, including both limiting FPOs, are studied, cf. Fig. 4.

Fig. 11 (c) and (d) shows the situation at $\tilde{E} = -1.4$ and $\tilde{F} = 0.5$, above the ionization saddle point. Here S^- is surrounded by an area filled with ionizing trajectories [6, 8, 42]. This ionizing region prevents the $T_2^{\mathrm{p,n}}$ from collapsing onto S^-. Yet, they still emanate from S^+.

Fig. 12 (a) shows the frequency ratios of 2- and 3-torus POs. For the 2-torus POs, the missing ratio $\tilde{\omega}_3/\tilde{\omega}_2$ is replaced with the stability angle that describes the dynamics transverse to the original torus, normalized by $2\pi w_2$. For the FPOs this angle is given by $\phi_1 - \phi_2$. The surroundings of a long stable PO can rotate multiple times around the PO during one period. Stability angles, however, can be calculated only modulo 2π. Therefore an integer number of 2π needs to be added to the stability angles of long POs. These stability angles arise in the w_3' coordinate system and thus need to be transformed with the inverse of Eq. (11). From Fig. 12 (a) it becomes apparent that the T_3 approach the T_2 in a suitable limit just as the T_2 approach the FPOs.

Frequency maps such as Fig. 12(b) have been found in, e.g., [19, 45] to capture the essential dynamics of a multi-dimensional system. Their most prominent features are the resonance lines, each of which is given by a resonance condition of the form

$$\sum_{i=1}^{f} m_i \tilde{\omega}_i = 0 \qquad (18)$$

with integer coefficients m_i. Their significance arises from the fact they they represent cantori that act as partial barriers to phase space transport. Diffusive trajectories such as those used in [19, 45] will stick to the cantori for a long time before leaving their neighborhood and thereby cause the prominence of the corresponding resonance lines in the frequency map.

The periodic orbits shown in Fig. 12 are the remnants of fully resonant tori, on which $f - 1$ independent resonance conditions of the form (18) are satisfied. (They can be derived from the condition (5)). 3-torus POs, therefore, will be located at the intersections of two resonance lines in the frequency map. Since POs are non-wandering, they belong to the rigid background through which the diffusion of generic trajectories takes place [10]. As Fig. 12 clearly shows, the set of POs presents the web of dominant resonances just as clearly as the set of diffusive trajectories that is customarily used.

The three action variables that characterize the 3-torus POs are displayed in Fig. 13 for the T_3^{p} family as functions of the two independent frequency ratios $\tilde{\omega}_1/\tilde{\omega}_2$ and $\tilde{\omega}_3/\tilde{\omega}_2$. They were calculated from Eq. (15) as described above. The action variables $\tilde{I}_1$ and $\tilde{I}_2$ obtained from the 3-torus POs converge towards those found for the 2-torus POs, while $\tilde{I}_3$ tends to zero as the lower boundary is approached. We thus find all three criteria of Sec. III satisfied in this higher-dimensional situation: The transverse frequency ratio $\tilde{\omega}_3/\tilde{\omega}_2$ of the T_3^{p} tends to the transverse stability angle of the T_2^{p}, the longitudinal action variables $\tilde{I}_1$ and $\tilde{I}_2$ of the 3-tori approach those of the 2-tori, and
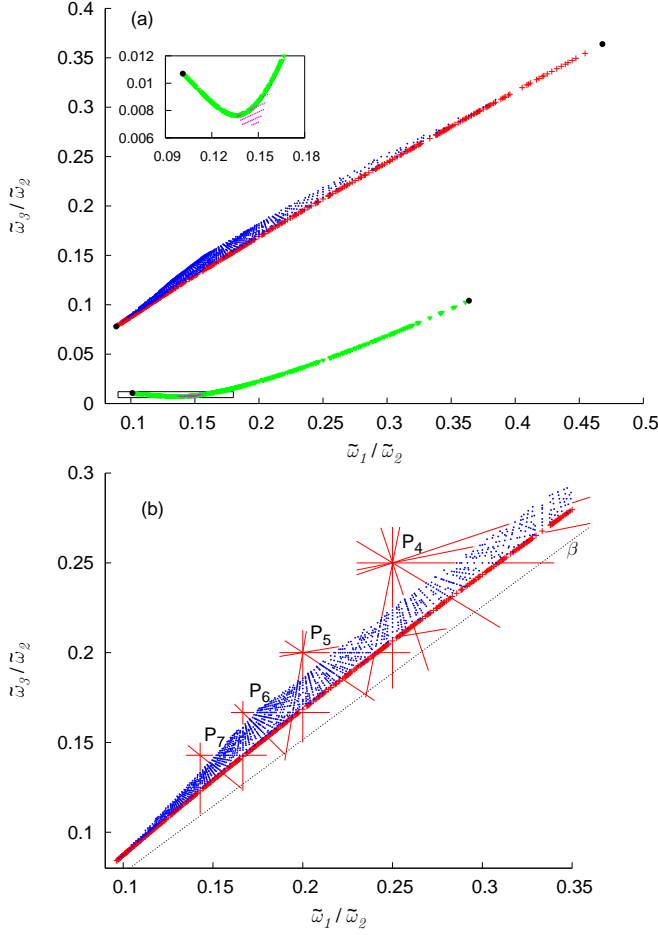
Figure 13: Action variables for the T_3^p family at $\tilde{E} = -1.4$, $\tilde{F} = 0.5$. At the lower boundary, where the T_3^p are bounded by the T_2^p, $\tilde{I}_3$ tends to zero while $\tilde{I}_{1,2}$ tend toward the values obtained from the 2-torus POs. For clarity the dotted line β from Fig. 12 (b) has been subtracted on the vertical axis.

VI. TORUS QUANTIZATION

The action variables calculated in the preceding paragraph provide the basis for an Einstein-Brillouin-Keller (EBK) torus quantization of the hydrogen atom in crossed electric and magnetic fields. The way of recording a quantum spectrum that is best suited to semiclassical investigations of atomic spectra is scaled-energy spectroscopy, which has for that reason been used in most experimental and theoretical work [2, 7, 46]. It offers the advantage that the underlying classical dynamics does not change across the spectrum. A scaled spectrum consists of those values of the scaling parameter $B^{-1/3}$ that characterize the quantum states for given scaled energy $\tilde{E}$ and scaled electric field strength $\tilde{F}$.

The phase space volume filled by 3-torus POs from the T_3^p family is considerably larger than the volume filled by T_3^n, as can be seen by the number of respective POs for example in Fig. 1. Thus, the largest part of the spectrum is also obtained from the quantization of the actions belonging to T_3^p.

The EBK quantization condition reads [25, 26, 27, 28, 29]:

$$I_i = \oint_{\gamma_i} \mathbf{p}\,d\mathbf{q} = 2\pi\hbar\left(n_i + \frac{\alpha_i}{4}\right)\ , \qquad i = 1,\ldots,f, \quad (19)$$

where the γ_i are the fundamental loops on the torus used in the definition (3) of the action variables, n_i are integer quantum numbers and α_i the corresponding Maslov indices. As shown above, one can obtain the action integrals from PO data without having to determine the paths γ_i. In our case, we calculate the scaled action variables $\tilde{I}_i$ which need to be rescaled to obtain the true actions $I_i = \tilde{I}_i B^{-1/3}$. Thus, the quantization condition

Figure 12: (a) Frequency map for N-torus POs at $\tilde{E} = -1.5$, $\tilde{F} = 0.5$. The 3-torus POs T_3^p (blue crosses) and T_3^n (magenta diamonds) are bounded by the corresponding 2-torus POs T_2^p (red plus symbols) and T_2^n (green triangles). The 2-torus POs in turn are bounded by the FPOs $S^\pm$ (black dots). (b) The T_3^p at $\tilde{E} = -1.4$, $\tilde{F} = 0.5$ with some of the most prominent resonance lines highlighted. They intersect in the points $P_i = \left(\frac{1}{i}, \frac{1}{i}\right)$.

the transverse action variable $\tilde{I}_3$ vanishes. We can therefore conclude that the T_2^p family serves as an organizing center for the T_3^p, and we can identify the degree of freedom corresponding to $\tilde{I}_3$ as being transverse to the family of 2-tori. Similar results can be obtained for the collapse of the T_3^n family onto T_2^n, thus giving a full justification for all relations depicted in Fig. 4.

Because of these relations, additional data points at the lower boundary in Fig. 13 can be obtained from the T_2^p (and are included in the figure). For these, the missing frequency ratio $\tilde{\omega}_3/\tilde{\omega}_2$ is replaced with the stability angle according to Fig. 12, the action variables $\tilde{I}_1$ and $\tilde{I}_2$ are taken from Fig. 11, and $\tilde{I}_3$ is zero.
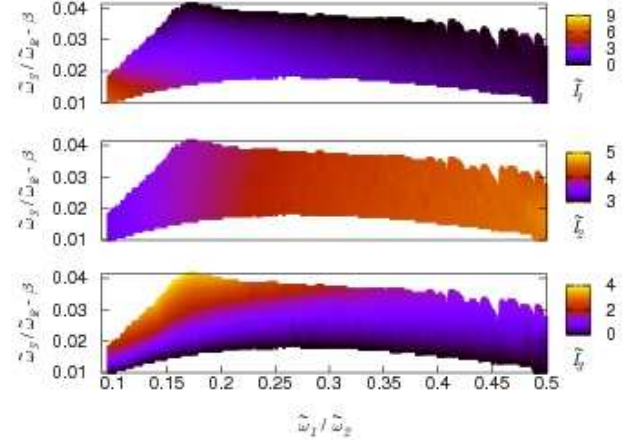
reads, with $\hbar = 1$ in atomic units:

$$\tilde{I}_i \left(\frac{w_1}{w_2}, \frac{w_3}{w_2} \right) B^{-1/3} = 2\pi \left(n_i + \frac{\alpha_i}{4} \right). \qquad (20)$$

We derive the Maslov indices α_i from two simple considerations: In the limit of small $\tilde{I}_1$ and $\tilde{I}_3$, the action variable $\tilde{I}_2$ and its conjugate angle correspond to the motion along the elliptic FPOs, which clearly has rotational character and requires $\alpha_2 = 0$. The other two modes are transverse to this fundamental motion and are thus expected to have vibrational character, which leads to $\alpha_1 = \alpha_3 = 2$.

Inverting Eq. (20) to calculate $B^{1/3}$ gives:

$$B^{-1/3} = \frac{2\pi \left(n_i + \frac{\alpha_i}{4} \right)}{\tilde{I}_i \left(\frac{w_1}{w_2}, \frac{w_3}{w_2} \right)}. \qquad (21)$$

A quantization condition for the scaled spectrum is obtained by observing that $B^{-1/3}$ must take the same value for all three degrees of freedom. We can thus calculate the frequency ratios corresponding to the state with given quantum numbers n_1, n_2, n_3 from the following set of equations

$$\frac{\tilde{I}_1 \left(\frac{w_1}{w_2}, \frac{w_3}{w_2} \right)}{2\pi \left(n_1 + \frac{\alpha_1}{4} \right)} - \frac{\tilde{I}_2 \left(\frac{w_1}{w_2}, \frac{w_3}{w_2} \right)}{2\pi \left(n_2 + \frac{\alpha_2}{4} \right)} = 0, \qquad (22)$$

$$\frac{\tilde{I}_1 \left(\frac{w_1}{w_2}, \frac{w_3}{w_2} \right)}{2\pi \left(n_1 + \frac{\alpha_1}{4} \right)} - \frac{\tilde{I}_3 \left(\frac{w_1}{w_2}, \frac{w_3}{w_2} \right)}{2\pi \left(n_3 + \frac{\alpha_3}{4} \right)} = 0 \qquad (23)$$

and then compute the value of the scaling parameter from (21).

Fig. 14 shows the EBK spectrum obtained from the quantization of the T_3^{p}. The low-lying states are labeled with the semiclassical quantum numbers (n_1, n_2, n_3). The manifolds of constant n_2, corresponding to the quantization of $\tilde{I}_2$, determine the principal series discernible in the spectrum. The n_2-manifolds overlap for $n_2 > 4$. For given n_2, n_1 ranges from 0 to $2n_2 - 2$, giving a total number of $2n_2 - 1$ subseries. The number of states within one subseries is $n_2 - \mathrm{Int} \left[\frac{n_1}{2} \right]$. Subseries are identified by a constant value of $n_1 + n_3$. The states within one subseries are labeled by n_3, beginning with 0 for the highest state.

Fig. 14 demonstrates that the spectrum derived from the quantization of the T_3^{p} is in very good agreement with the exact quantum spectrum obtained as in, e.g., [12, 46, 47]. The energy levels can be characterized in terms of three quantum numbers n, q, k, which were first introduced in perturbation theory [48]: The principal quantum number n identifies the principal series. The second quantum number q runs from $-(n-1), \ldots, +(n-1)$ with increasing energy and corresponds to the subseries. Finally, k counts the states within a subseries and runs from 0 to $n - |q| - 1$. A line-by-line comparison between the semiclassical and the exact quantum spectrum

n	q	k	n_2	n_1	n_3	$B_{\mathrm{qm}}^{-1/3}$	$B_{\mathrm{EBK}}^{-1/3}$
1	0	0	1	0	0	1.6773	1.6758
2	-1	0	2	0	0	3.0754	3.0761
2	0	1	2	0	1	3.3442	3.3448
2	0	0	2	1	0	3.3632	3.3615
2	1	0	2	2	0	3.5671	3.5671
3	-2	0	3	0	0	4.4309	4.4320
3	-1	1	3	0	1	4.7528	4.7526
3	-1	0	3	1	0	4.7888	4.7883
3	0	2	3	0	2	5.0134	5.0150
3	0	1	3	1	1	5.0279	5.0273
3	0	0	3	2	0	5.0500	5.0487
3	1	1	3	2	1	5.2428	5.2437
3	1	0	3	3	0	5.2619	5.2610
3	2	0	3	4	0	5.4435	5.4445

Table I: Semiclassical and exact eigenvalues of the scaling parameter at $\tilde{E} = -1.4$ and $\tilde{F} = 0.5$.

as in Table I yields the following correspondence between the torus quantum numbers n_1, n_2, n_3 and the quantum numbers n, q, k:

$$\begin{aligned} n &= n_2, \\ q &= (n_1 + n_3 + 1) - n_2, \qquad (24) \\ k &= n_3. \end{aligned}$$

Since $\tilde{I}_2$ corresponds to the fastest rotation, it comes as no surprise that the semiclassical n_2 represents the principal quantum number n.

For large n_2, the frequency ratios calculated from Eqs. (22) and (23) for the lowest peaks in the central subseries ($n_1 + n_3 \approx n_2$) lie outside the frequency range covered by the T_3^{p}. These peaks belong to the T_3^{n} family. However, the boundary of frequency ratios, especially in regions where few POs are available for the calculation of the action variables, is sometimes not clear-cut, which leads to a fuzzy boundary between the states of T_3^{p} and those of T_3^{n}. Fig. 15 shows a spectrum for a single subseries where the lowest states are taken from the quantization of the T_3^{n}. The quantization of the T_3^{n} requires $\alpha_1 = 0$ and yields a correspondence between torus quantum numbers and traditional quantum numbers that is different from (24). The comparison with the exact quantum spectrum in Fig. 15 shows excellent agreement, with the exception of the two right-most peaks. These states lie in a region of the plane of winding ratios where not many POs are known and the action variables can be calculated only to correspondingly lower accuracy.

VII. CONCLUSION

The hydrogen atom in crossed electric and magnetic fields presents long-standing challenges to both the dynamical-systems and the atomic-physics communities.
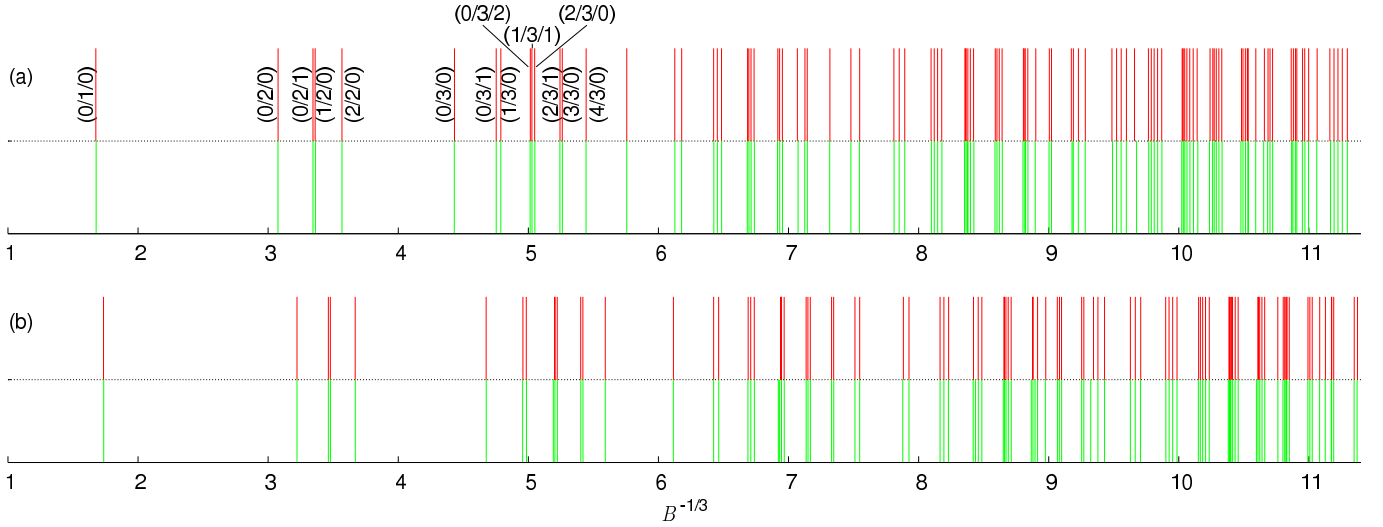
Figure 14: (a) The EBK spectrum as obtained from the quantization of the T_3^{p} (upper half, red) at $\tilde{E} = -1.4$ and $\tilde{F} = 0.5$ compared to the exact quantum-mechanical spectrum (lower half, green). The first three n_2-manifolds are labeled with (n_1, n_2, n_3). (b) Spectra at $\tilde{E} = -1.5$, $\tilde{F} = 0.5$.
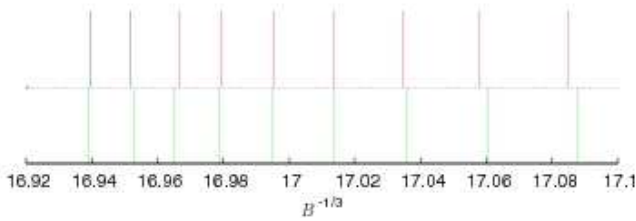

Figure 15: The quantization of the T_3^{n} family (blue) gives the two left-most peaks in the $n_2 = 10$ and $n_1 + n_3 = 10$ ($n = 10$, $q = 1$) subseries showing a good agreement with the exact quantum spectrum (green). The other peaks result from the quantization of the T_3^{p} (red). The slight discrepancies of the peaks on the right are due to numerical inaccuracies in the interpolation procedure.

In this work we have addressed both issues. From the viewpoint of dynamical systems we have demonstrated the power of periodic orbits when they are used as a probe to the intricacies of the geometrical and dynamical structures in phase space. Being the remnants of broken tori, periodic orbits can be used to establish a complete hierarchy of these phase space structures. At energies slightly below and slightly above the ionization saddle point of the crossed-fields hydrogen atom we established this hierarchy as follows. Three fundamental periodic orbits [4] that do not arise from the breakup of a higher-dimensional torus represent the 1-tori in the hierarchy. Two of them serve as organizing centers for two families T_2^{p} and T_2^{n} of 2-torus POs. The periodic orbits located in the x-y symmetry plane form the T_2^{p} family. The 2-torus POs themselves were found to be limiting cases of two families T_3^{p} and T_3^{n} of 3-torus POs.

Having established the hierarchy of POs, we calculated the individual action variables for the different families

of POs. This knowledge provides the basis for the semiclassical calculation of the atomic spectrum using EBK quantization. Our results are in good agreement with the exact quantum mechanical spectrum.

Because the classification of POs by winding numbers relies only on the existence of a hierarchy of broken tori, which is a common feature in many non-integrable Hamiltonian systems, it will be applicable to other challenging systems. In particular, previous experience on the hydrogen atom in a magnetic field [49] has shown that a semiclassical approximation that is derived in a near-integrable setting can successfully describe quantum states even deep in the mixed regular-chaotic regime. It is therefore to be expected that our quantization scheme will still be useful at appreciably higher field strengths than were considered here.

Appendix A: THE PERIODIC-ORBIT SEARCH

Due to the Coulomb singularity in the Hamiltonian (1), a straightforward numerical integration of the trajectories is unfeasible. To overcome this difficulty, we use the Kustaanheimo-Stiefel regularization [50, 51] and integrate in *four-dimensional* position and momentum co-

ordinates **u** and **p**. The equations of motion in KS coordinates with respect to a pseudotime parameter τ are free of singularities (see, e.g., [47]).

We describe the search for periodic orbits as a root-finding problem. A PO is identified by a starting point $P_i = (\mathbf{u}, \mathbf{p})_i$ in phase space and by its pseudotime period τ. Given an initial guess for P_i and τ, we calculate the final point P_f of the trajectory by integrating the equations of motion for a time τ and then use a Newton-like method to modify P_i (within the energy shell) and τ so that $P_f = P_i$. Specifically, we use a Powell-hybrid root-finding method [44] for this task.

The initial guesses required by the root-finder are obtained as follows: we fix a Poincaré surface of section in phase space. Initial guesses for P_i are chosen on an equidistant grid on this four-dimensional surface. Starting from each of these points, we integrate the equations of motion until the trajectory returns to the neighborhood of its starting point (or a prescribed maximum period is exceeded). The time it takes for the trajectory to come back close to its starting point serves as the initial guess for the period τ.

Like any other numerical PO search, this algorithm is not guaranteed to find all POs. It does not require any prior knowledge of the dynamics, which we extract from the POs *a posteriori*, even if the data set is incomplete.

[1] G. Wiebusch, J. Main, K. Krüger, H. Rottke, A. Holle, and K. H. Welge, Phys. Rev. Lett. **62**, 2821 (1989).
[2] G. Raithel, M. Fauth, and H. Walther, Phys. Rev. A **44**, 1898 (1991).
[3] G. Raithel and H. Walther, Phys. Rev. A **49**, 1646 (1994).
[4] E. Flöthmann, J. Main, and K. H. Welge, J. Phys. B **27**, 2821 (1994).
[5] E. Flöthmann and K. H. Welge, Phys. Rev. A **54**, 1884 (1996).
[6] T. Uzer and D. Farrelly, Phys. Rev. A **52**, R2501 (1995).
[7] C. Neumann, R. Ubert, S. Freund, E. Flöthmann, B. Sheehy, K. H. Welge, M. R. Haggerty, and J. B. Delos, Phys. Rev. Lett. **78**, 4705 (1997).
[8] J. von Milczewski, D. Farrelly, and T. Uzer, Phys. Rev. A **56**, 657 (1997).
[9] D. M. Wang and J. B. Delos, Phys. Rev. A **63**, 043409 (2001).
[10] J. von Milczewski, G. H. F. Diercksen, and T. Uzer, Phys. Rev. Lett. **76**, 2890 (1996).
[11] R. H. Cushman and D. A. Sadovskií, Physica D **142**, 166 (2000).
[12] J. Main and G. Wunner, Phys. Rev. Lett. **69**, 586 (1992).
[13] G. Stania and H. Walther, Phys. Rev. Lett. **95**, 194101 (2005).
[14] M. M. Dignam and J. E. Sipe, Phys. Rev. B **45**, 6819 (1992).
[15] E. Lee, A. Puzder, M. Y. Chou, T. Uzer, and D. Farrelly, Phys. Rev. B **57**, 12281 (1998).
[16] H. Poincaré, *Les méthodes nouvelles de la mécanique céleste*, vol. 1 (Imprimerie Gauthier-Villars et fils, Paris, 1892).
[17] V. Szebehely, *Theory of orbits* (Academic Press, 1967).
[18] F. Gabern and À. Jorba, Discrete Contin. Dynam. Systems Series B **1**, 143 (2001).
[19] D. Robin, C. Steier, J. Laskar, and L. Nadolski, Phys. Rev. Lett. **85**, 558 (2000).
[20] G. Kawahara and S. Kida, J. Fluid. Mech. **449**, 291 (2001).
[21] M. Joyeux and L. Michaille, ACH – Models in Chemistry **134**, 573 (1997).
[22] R. Prosmiti and S. C. Farantos, J. Chem. Phys. **118**, 8275 (2003).
[23] F. J. Arranz, R. M. Benito, and F. Borondo, J. Chem. Phys. **123**, 044301 (2005).
[24] O. Hahn, J. M. G. Llorente, and H. S. Taylor, J. Chem. Phys. **94**, 2608 (1991).
[25] A. Einstein, Verh. Dtsch. Phys. Ges. **19**, 82 (1917).
[26] L. Brillouin, J. Phys. Radium **7**, 353 (1926).
[27] J. B. Keller, Ann. Phys. (NY) **4**, 180 (1958).
[28] I. C. Percival, Adv. Chem. Phys. **36**, 1 (1977).
[29] M. Brack and R. K. Bhaduri, *Semiclassical physics* (Westview Press, 2003).
[30] P. J. Mohr and B. N. Taylor, Rev. Mod. Phys. **77**, 1 (2005), p. 71.
[31] H. Friedrich, in *Atoms and Molecules in Strong External Fields*, edited by P. Schmelcher and W. Schweizer (Plenum Press, New York, 1998), pp. 153–167.
[32] V. I. Arnold, *Mathematical Methods of Classical Mechanics* (Springer, 1989).
[33] A. J. Lichtenberg and M. A. Lieberman, *Regular and Chaotic Dynamics* (Springer, 1992).
[34] J. von Milczewski and T. Uzer, Phys. Rev. A **56**, 220 (1997).
[35] E. Tannenbaum and E. J. Heller, J. Phys. Chem. A **105**, 2803 (2001).
[36] S. Chapman, B. C. Garrett, and W. H. Miller, J. Chem. Phys. **64**, 502 (1976).
[37] C. C. Martens and G. S. Ezra, J. Chem. Phys **86**, 279 (1987).
[38] M. Born, *The mechanics of the atom* (Bell, London, 1927).
[39] G. D. Birkhoff, Mem. Pont. Acad. Sci. Novi Lyncaei **1**, 85 (1935).
[40] H. Kook and J. D. Meiss, Physica D **35**, 65 (1989).
[41] S. Gekle, J. Main, T. Bartsch, and T. Uzer, Phys. Rev. Lett. **97**, 104101 (2006).
[42] C. Jaffé, D. Farrelly, and T. Uzer, Phys. Rev. A **60**, 3833 (1999).
[43] J. E. Howard and R. S. MacKay, J. Math. Phys. **28**, 1036 (1987).
[44] We use an implementation from The Numerical Algorithms Group, www.nag.com.
[45] J. Laskar, Physica D **67**, 257 (1993).
[46] J. Rao, D. Delande, and K. T. Taylor, J. Phys. B **34**, L391 (2001).
[47] J. Main and G. Wunner, J. Phys. B **27**, 2835 (1994).
[48] P. A. Braun and E. A. Solovev, Sov. Phys. JETP **59**, 38 (1984).
[49] J. Main and G. Wunner, Phys. Rev. Lett. **82**, 3038 (1999).

[50] P. Kustaanheimo and E. Stiefel, J. Reine Angew. Mathematik **218**, 204 (1965).

[51] E. Stiefel and G. Scheifele, *Linear and regular celestial mechanics* (Springer, 1971).